Supplementary Information (SI) for Nanoscale.

Supplementary: Bimodal Interfacial Charge Transfer in Quantum Dot Heterostructures Revealed by Donor-/Acceptor-Specific Broadband Transient Absorption Spectroscopy

Conner Dykstra[1], Thomas C. Rossi[1,2], Michael Enright[3], Josh Vura-Weis[1], and Renske M. van der Veen[1,2]

[1]UIUC
[2]HZB
[3]UIUC bis

June 30, 2025

1 Methods

1.1 ZnO Nanorods

Initially, a seed layer of ZnO is deposited on two side polished 001-cut quartz purchased from MTI inc (10 x 10 x 0.5 mm). The quartz substrate is first cleaned by sonication in acetone for 15 minutes, followed by another sonication in ethanol for 15 minutes. 200 μL of a 375 mM ethanolic solution of zinc acetate and ethanol amine was spin coated onto the cleaned quartz substrates at 3000 rpm, which were then annealed in a tube furnace under argon. During annealing, the sample was first heated to 150 C and held there for 10 minutes, then heated to 400 C and annealed for 20 minutes with a 10 C/min ramp rate. Before growing, the vessel was cleaned with 1 M hydrochloric acid, then washed with saturated sodium bicarbonate. The

ZnO nanorods were then grown in an aqueous 15 mM solution of Zn nitrate and hexmethylenetetramine (HMTA) at 90 C, for 45 minutes. This produces a dense array of nanorods approximately 380 nm long and 60 nm wide.[1, 2]

1.2 CdSe Quantum Dots

CdSe nanocrystals were synthesized similar to previously reported procedures.[3–6] Cadmium oxide (CdO, 99.9%) and selenium (Se, 100 mesh, 99.999%), were obtained from Sigma Aldrich and used as received. Oleic acid (OA, 90%) and 1-octadecene (1-ODE, 90%) were obtained from Sigma Aldrich and used after purification by distillation. In a 50-mL, 3-neck flask, 300 mg CdO, 2 mL OA, and 20 mL 1-ODE were degassed under vacuum while stirring for 10 min. Nitrogen was introduced and the mixture was heated to 250 °C until the solution turned clear, signifying the formation of cadmium oleate. Upon turning clear, the temperature was reduced to 120 °C and 100 mg of Se powder was added via a solid addition funnel, and the solution was heated to 185 °C for 2.3 nm CdSe or 215 °C for 2.6 nm CdSe, leading the color to evolve from clear to yellow to orange indicating the nucleation and growth of CdSe quantum dots until the quantum dots reached the desired size.

For 4.2 nm CdSe - in a 50-mL, 3-neck flask, 500 mg CdO, 3.33 mL OA, and 20 mL 1-ODE were degassed under vacuum while stirring for 10 min. Nitrogen was introduced and the mixture was heated to 250 °C until the solution turned clear, signifying the formation of cadmium oleate. Upon turning clear, the temperature was reduced to 120 °C and 100 mg of Se powder was added via a solid addition funnel, and the solution was heated to 240 °C, leading the color to evolve from clear to yellow to orange indicating the nucleation and growth of CdSe quantum dots. Upon reaching 240 °C, 1 mL of TOP-Se (prepared from 67 mg selenium powder in 1 mL trioctylphosphine) is added dropwise. The outcome is quantum dots with an absorbance of 590 nm.

Once the quantum dots reached the appropriate size, the heat was removed, and the reaction was quenched in a room-temperature oil bath. The CdSe quantum dots were purified in an N_2 filled glovebox by three cycles of precipitation and redissolution with a centrifuge at 7,000 rpm for 10 min using pentane as the solvent and ethanol as the antisolvent.

The size of the quantum dots was determined from the published sizing curve of Jasieniak et al. [7]:

$$D(nm) = 59.60816 - 0.54736\lambda + 1.8873e^{-3}\lambda^2 - 2.85743e^{-6}\lambda^3 + 1.62974e^{-9}\lambda^4 \quad (1)$$

Where λ is the peak of the E_{1S} transition, which is the lowest energy optical transition in CdSe quantum dots, and D is the diameter of the quantum dots. The first excitonic transition is at 485 nm, 515 nm, and 590 nm corresponds to quantum dots of size 2.3 nm (blue), 2.6 nm (green), 4.2 nm (red) quantum dots.

1.3 Sensitized Nanorods

Exchanging the native organic ligands was done with a biphasic mixture of 100 μL MPA dissolved in water and 60 nmols of CdSe QDs dispersed in hexane. The mixture was shaken and lightly heated for 10 - 15 minutes, or until phase transfer had completed. The mixture was washed three times with hexane, then the QD's were aggregated with excess acetonitrile and centrifuged. After discarding the supernatant, the purified QDs were redispersed in 2-3 mLs of methanol.[8] Conjugation of the QD's with the ZnO was done by first heating the ZnO in a vacuum oven at 70 C, then immediately immersing the ZnO in the QD solution. The mixture was kept at 50 C under nitrogen, and in the dark, for approximately 12 hours. The ZnO was then washed with ethanol and stored under nitrogen in the dark.

2 Exciton Population

The relevant fluence ranges used during measurements was estimated with equation 2, while targeting a low number of excitons per quantum dot, at 0.2. The distribution of excitonic states is shown in figure 1, which is derived from the following calculations:

$$<N>= \frac{\phi(1-10^{-OD_{\text{pump}}})}{[\text{QD}] * V_{\text{int}} * N_{\text{A}}} \quad (2)$$

<N> is the average number of excitons per quantum dot, ϕ is the photon flux in photons/pulse, OD_{pump} is the OD of the sample at the pump wavelength, [QD] is the concentration of the quantum dots in molarity, and V_{int} is the interaction volume of the pump laser with the sample, and N_A is Avogadro's number. The photon flux is determined by converting the peak power per pulse to photons using the measured pump spectrum as the photon energy, which is 2.41 eV. V_{int} is calculated by taking

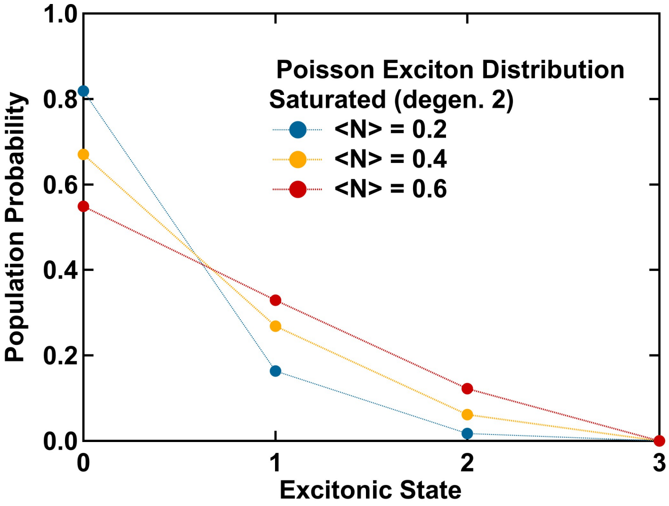

Figure 1: The distribution of excited quantum dot states, as calculated using equations 2 and 3. Each trace shows probability for the quantum dot ensemble to be either unexcited, singly excited, or doubly excited for a given average number of excitons. The blue trace shows <N> of 0.2, the yellow trace shows <N> of 0.4, and the red trace shows <N> of 0.6. Since CdSe has a degeneracy of 2 at the bandgap, where they are being excited, no quantum dot will be more than doubly excited. Even at the lowest excitation employed here, there is still a nonzero population of doubly excited quantum dots.

the spot size of the laser and multiplying by the ZnO nanorod length, estimated at 380 nm from SEM images. From <N>, the distribution of excitonic states can be calculated with Poisson statistics according to equation 3, while taking into account the degeneracy at the band gap:

$$\begin{aligned} N_i &= \frac{< N >^i * e^{-<N>}}{i!} \\ N_2 &= 1 - \sum_{n=0}^{i} N_i \\ N_{i>2} &= 0 \end{aligned} \tag{3}$$

N_i is the fraction of QDs with a given i excitonic state, and N_2 is the doubly excited state. The band edge degeneracy can be taken into account by requiring the sum

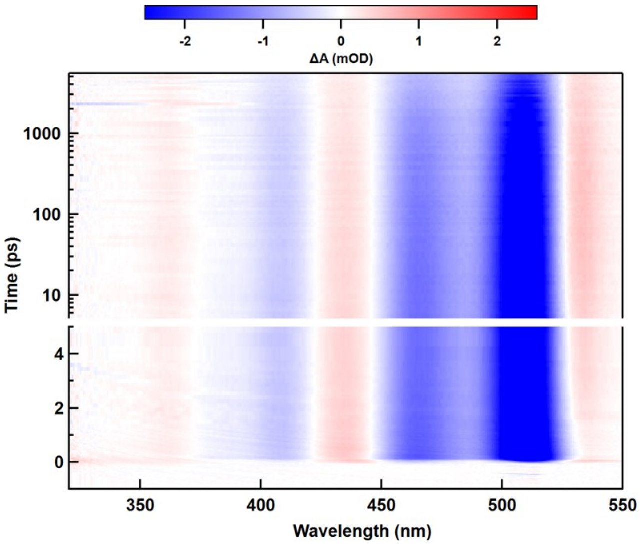

Figure 2: 2D dataset of transient absorption in hexane of 2.6 nm CdSe quantum dots with a target fluence of 20 μJ/cm^2.

$\sum_{n=0}^{2} N_i = 1$.[9] The fluences used in these experiments aimed to minimize 2PA and QD degradation, while also exciting a significant fraction of quantum dots. All charge injection experiments were measured with an average excitation of 0.2, where the population of excited states are shown in figure 1 for three different <N>. For excitations less than 1 photon per quantum dot the majority of quantum dots are unexcited, although even at low average excitations an appreciable number of multi-excitonic states can be expected. An average excitation of 0.2 gives 1.75% of quantum dots being doubly excited, with 16.4% of quantum dots being singly excited. Quantum dots with biexcitonic states then compose approximately 10% of the excited quantum dot states, which can account for as much as 20% of the total signal at the band gap. Since the spectrum changes rapidly due to charge transfer, it's not possible to disentangle the dynamics from the different excitonic states. <N> of 0.2 is the lowest excitation achievable considering experimental constraints (e.g. quantum dot concentration, laser power stability, and signal amplitude).

3 Solution Phase CdSe

Figure 2 shows the transient absorption spectrum of CdSe quantum dots in hexane with native oleic acid ligands, excited at 513 nm with 20 μJ/cm^2 to achieve an <N >of 0.2. The band gap excitation shows a strong ground state bleach at the first excitonic transition of 515 nm, with a max amplitude of -3 mOD. A corresponding bleach of the second excitonic transition can also be seen at 460 nm because it shares the same electronic state as the first transition. At lower wavelengths there are derivative like features due to a red shift of the absorption spectrum into a biexcitonic state (400 - 450 nm), along with an excited state absorption just to the red of the first excitonic peak (540 nm).[10] A low amplitude excited state absorption 150 μOD (ESA) is seen at the excitonic transition of ZnO (365 nm). As shown in the main text, this feature is not seen in the sensitized sample.

4 Two-Dimensional Data

Figures 3 through 5 show example two dimensional datasets for the 2.3 nm CdSe@ZnO, 2.6 nm CdSe@A-ZnO, and 4.2 nm CdSe@ZnO. Typical signal strengths were below 1 mOD. Excitation wavelengths were set for the peak of the first excitonic transition to minimize carrier cooling effects, which was 485 nm, 513 nm, and 590 nm for the three samples respectively. Fluences were targeted to maintain an identical Poisson distribution of $<N> \approx 0.2$, which corresponded to a fluence of 40 μJ/cm^2, 62 μJ/cm^2, 31 μJ/cm^2 respectively.

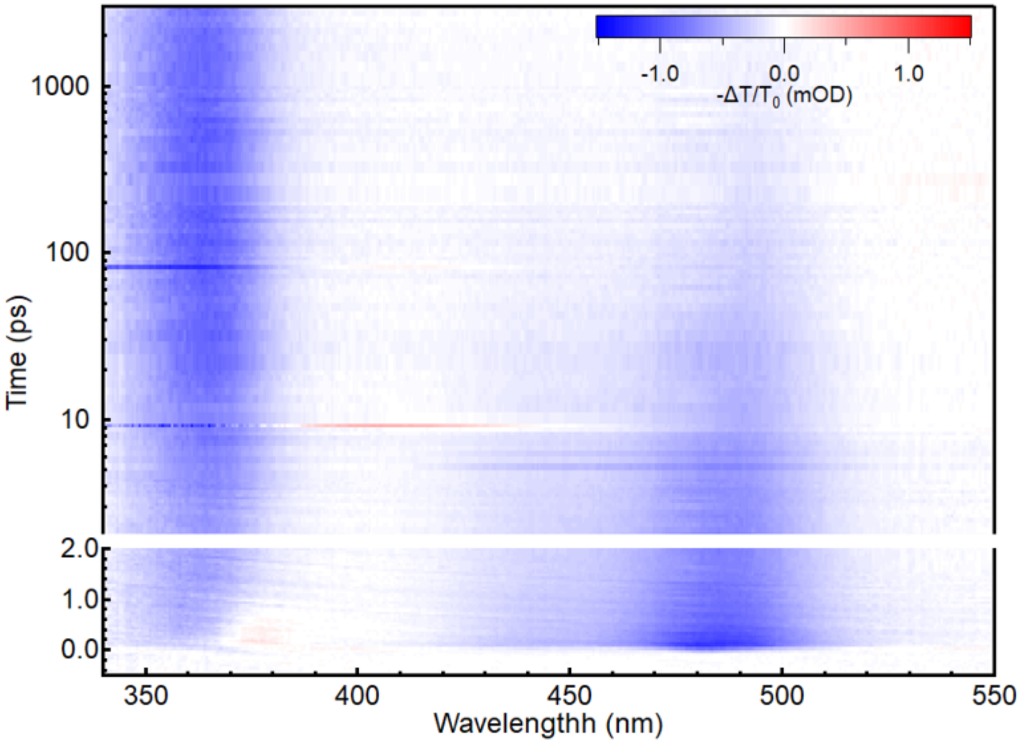

Figure 3: An example averaged UV (left) and visible (right) transient absorption dataset for 2.3 nm CdSe@ZnO excited at 485 nm. The bleach of the CdSe appears immediately at 485 nm, and decays quickly on the few ps timescale. The bleach feature of ZnO appears around 365 nm, and sees a fast evolution over the first 10 ps. There is evidence of two photon absorption, as seen by the immediate appearance of signal at 365 nm, with a rapid decay followed by a growth in signal from electron injection.

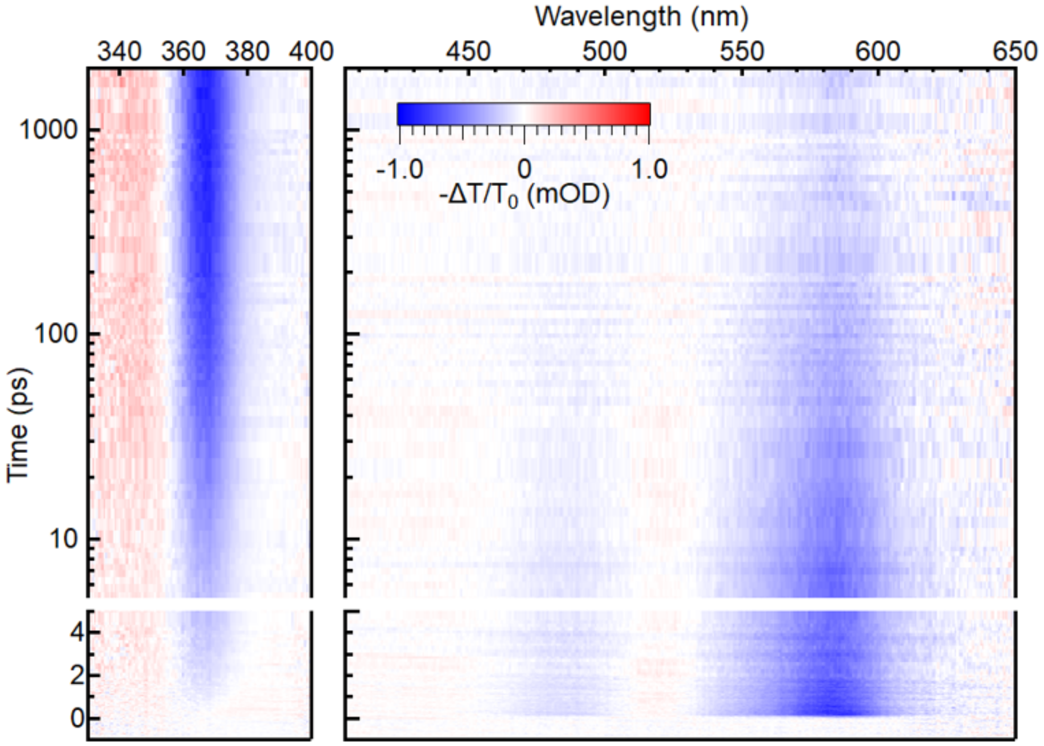

Figure 4: An example averaged UV (left) and visible (right) transient absorption dataset for 4.2 nm CdSe@ZnO excited at 590 nm. The bleach of the CdSe appears immediately at 590 nm, and decays slowly on the 10's of ps timescale. The bleach feature of ZnO appears around 365 nm, and sees a slow evolution over the first 100 ps.

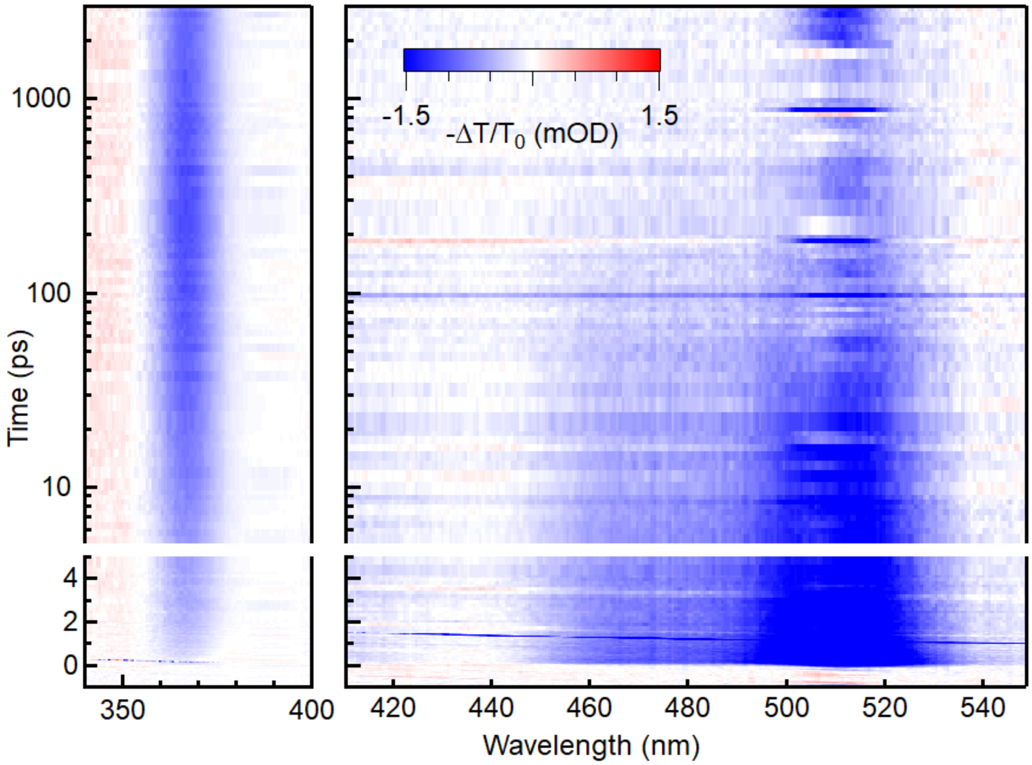

Figure 5: An example averaged UV (left) and visible (right) transient absorption dataset for 2.6 nm CdSe@A-ZnO excited at 513 nm. The bleach of the CdSe appears immediately at 513 nm, and decays on the few ps timescale. The bleach feature of ZnO appears around 365 nm, and grows in over the first ∼50 ps.

5 Akaike and Bayesian Information Criterion

There are many measures employed to estimate the quality of a fit to data, for which the reduced χ^2 is the most common. These best fit estimates penalize any given fit based on the number of parameters needed to reduce the sum of squared errors (SSE, equation 4). Two additional free parameters are added to the total number of parameters for each additional exponential component. The Akaike and Bayesian Information Criterion (AIC/BIC) are defined in equation 6 and 7:

$$SSE = \sum_{i=1}^{n} (y - y_i)^2 \tag{4}$$

$$\chi^2_{red} = SSE/(n - p) \tag{5}$$

$$AIC = n * \ln\left(\frac{SSE}{n}\right) + 2 * p \tag{6}$$

$$BIC = n * \ln\left(\frac{SSE}{n}\right) + p * \ln(n) \tag{7}$$

Where n is the number of data points, and p are the number of free variables.

This procedure is shown in figure 6 for the UV half-dataset. Each set of AIC/BIC values (orange and red, green and light blue, dark blue and pink) represents how well a given model fits the data. A lower AIC/BIC indicates the model fits the data better for the cost of including more parameters. The number of components is specifically the number of, in this case, rising exponentials used to fit the kinetic trace, while only considering the rising portion of the data. Going from 1 to 2 components then, the AIC/BIC values decrease significantly for all dataests. However, going from 2 to 3 components produces a slight increase in the AIC/BIC values for most of the datasets. 2 rising exponential components is then the ideal fit function for this half-dataset. Visible datasets which measure the CdSe are fitted with decaying exponential functions. Each additional exponential requires the inclusion of two more parameters: an amplitude and a time constant. The inclusion of an extra component is then justified by reaching the minimum AIC/BIC. A sum of exponentials model is then chosen for the half-dataset as a whole, without separating out individual spot datasets. Outlier spot-datasets were determined from the deviation of time constants from the weighted mean of the half-dataset. The AIC and BIC measures are most useful within similar classes of models, and is not necessarily reliable when

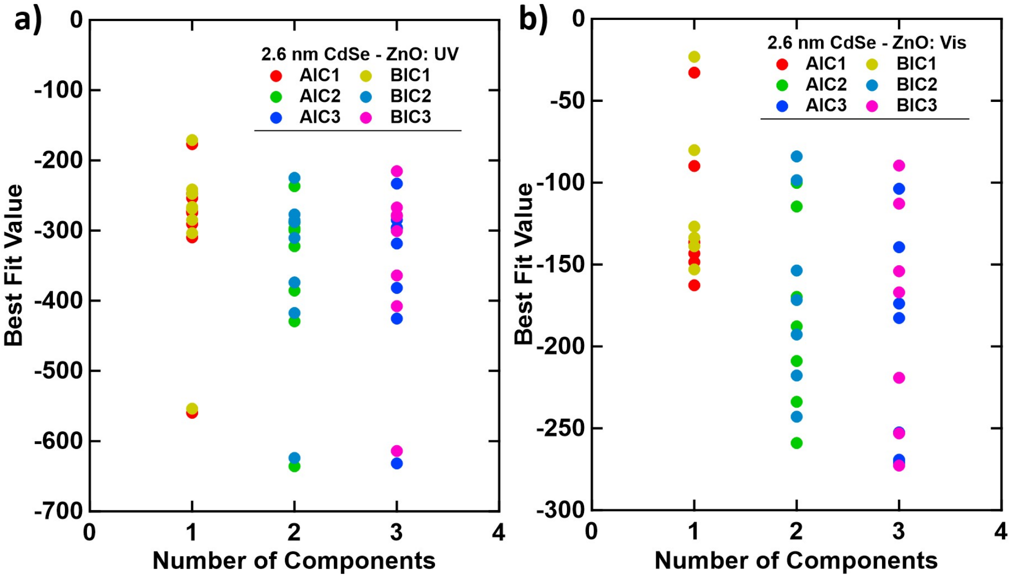

Figure 6: For 2.6 nm CdSe - ZnO with kinetic traces at a) 365 nm and b) 500 nm, the combined Akaike and Bayesian Information Criterion values, as calculated with equations 4 through 7, are presented. The complete UV and Vis half-datasets are represented, which encompasses all averaged spot datasets. The number of components is specifically the number of exponentially rising (or decaying) functions used to fit each dataset.

comparing models with different functional forms. A distribution of time constant rates may be required when $\sim$ 3 or more exponentials are needed to match the shape of the experimental kinetic decay, or when there is a reason for suspecting a distribution of energetic states (i.e. a distribution of QD sizes, or a distribution of binding motifs).[11] The most common way to account for, or test for a distribution of rates, is the stretched exponential or Kohlrausch rate law:[12]

$$S = A * e^{(-kt)^{\beta}} \tag{8}$$

Where β is a stretch factor determining the deviation from monoexponential kinetics. While popular, a difficulty with this approach is that multiple different ensembles of decay rates may give very similar experimental kinetics, making the extraction of a physical distribution very difficult.[12] Lastly, employing a stretched exponential also does not increase the best fit criterion, as shown in figure 7.

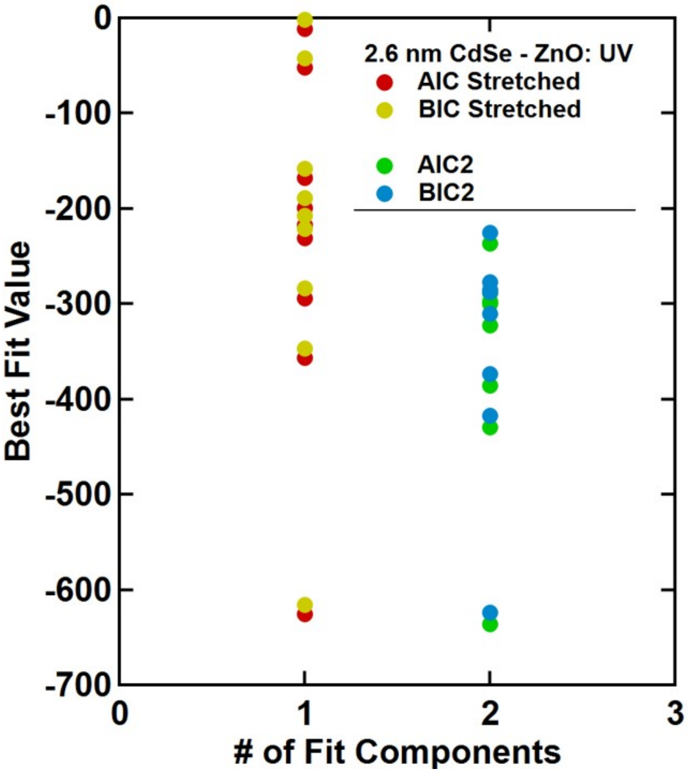

Figure 7: For 2.6 nm CdSe - ZnO with kinetic traces at 365 nm, the combined Akaike and Bayesian Information Criterion values, as calculated with equations 4 through 7, are presented. The complete UV half-dataset is represented, which encompasses all averaged spot datasets. A comparison is shown between a single exponential stretched function with a 2 component exponential sum, where the best fit criterion do no clearly improve with the application of a stretched exponential.

As demonstrated, the stretched exponential function has a worse fit as calculated with the chosen information criterion. However, these measures should be applied with caution when comparing different functional forms. A single stretched exponential was tested, as two stretched exponentials will be much more difficult to interpret compared to the more typical sum-of-exponentials.

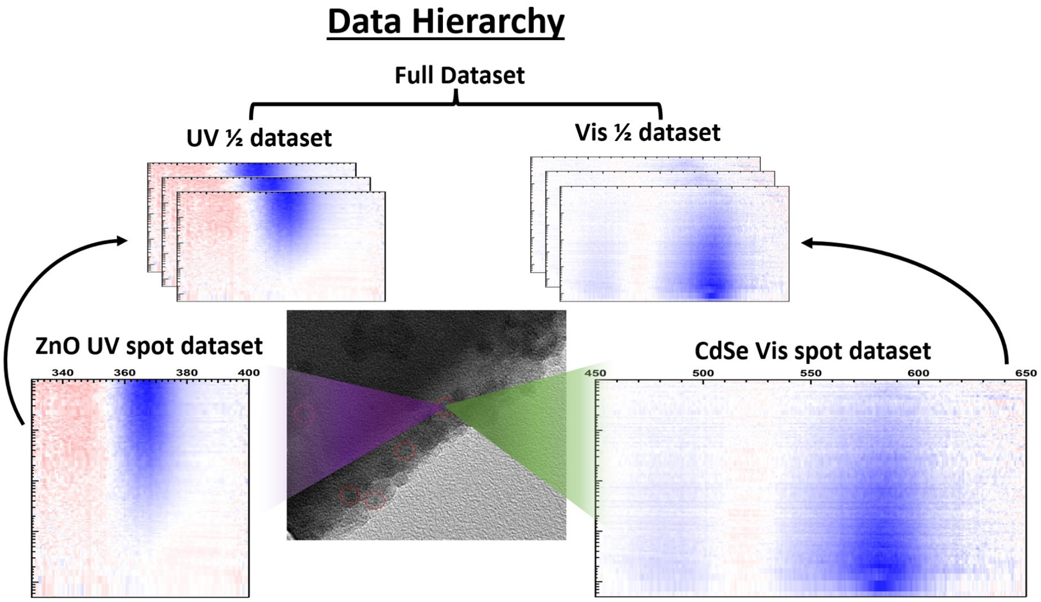

Figure 8: Shows the organization of data into three levels: the spatially and probe-region distinct spot-dataset, the probe-region specific half-dataset which encompasses the spot datasets, and the sample specific all-encompassing full dataset. Each spot dataset will be averaged until a reasonable signal-to-noise is achieved. Each half-dataset will contain a minimum of 5 spot datasets, which represents the ZnO or CdSe dynamics within that sample. Finally, the full dataset will contain two half-datasets and represents the system dynamics, as can be observed with optical spectroscopy, as a whole.

6 Data Hierarchy

The data is organized into a three level hierarchy, as shown in figure 8. The lowest level is the spot level, which are the individual measurements taken in either the UV or the visible probe region. Each spot was acquired in a spatially distinct point on the sample, with no spot being repeated between the UV probe and visible probe measurements. Each spot was measured between 3 and 6 times to be sufficiently averaged. Enough spots were measured to give a statistically relevant measure of the true kinetics of either the CdSe or ZnO. These spots are aggregated into a probe-region-specific dataset representing the ZnO (UV probe data) or CdSe (visible probe data), termed a half-dataset. Two half-datasets are then combined into a material level dataset that represents the complete dynamics in the QD - ZnO system. Prior to being assembled into a material dataset, each half-dataset was normalized to the maximum intensity.

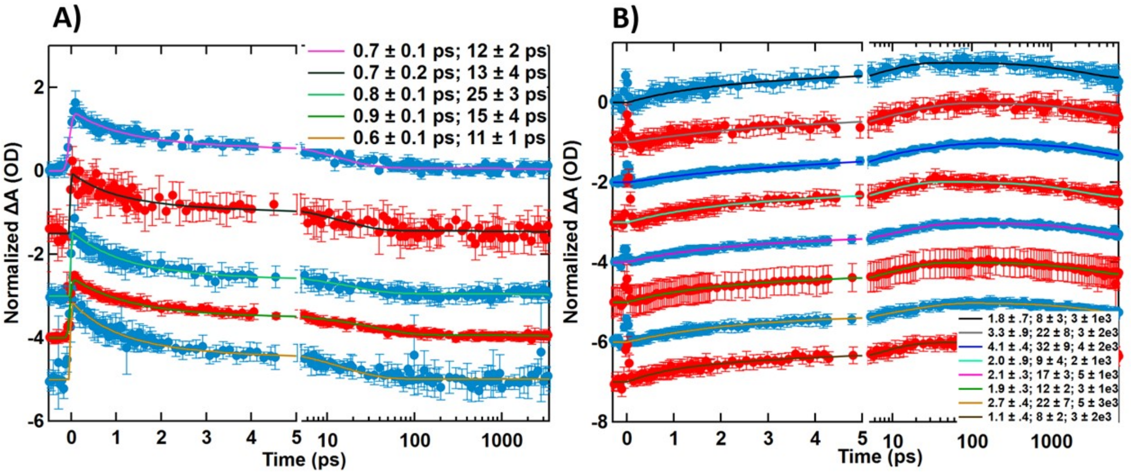

Figure 9: a) Raw normalized kinetic traces for 2.6 nm CdSe traces measured at 500 nm and binned over 2 nm. Solid lines are the fits to each trace for 2 exponential decays and 1 component that decays outside the spectral window. b) Raw normalized kinetic traces for the UV ZnO traces measured at 365 nm and binned over 1 nm. Solid lines are the fits to each trace for 2 exponential rises and 1 exponential decay. The averages and standard deviations are reported in the main text.

7 Raw Kinetic Traces and Fitting

The raw kinetic traces for UV and Visible measurements are shown in figure 10, along with the sum-of-exponential fits to each trace and corresponding time constants. The method for employed for these kinetic fits is described below. After kinetic fitting, the extracted time constants were averaged together while taking into account the standard deviation of the individual fits. The aggregate time constants and corresponding average is shown in 11. The sum of exponentials model is expressed by equation 9:

$$S = \Sigma_{i=0}^{n} A_i * e^{-k_i t} \tag{9}$$

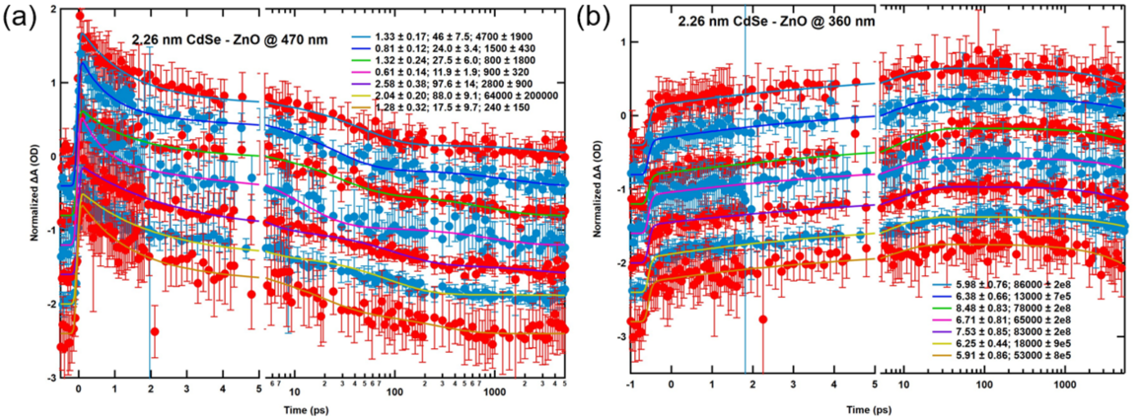

Figure 10: a) Raw normalized kinetic traces for 2.3 nm CdSe traces measured at 470 nm and binned over 2 nm. Solid lines are the fits to each trace for 2 exponential decays and 1 component that decays outside the spectral window. b) Raw normalized kinetic traces for the UV ZnO traces measured at 360 nm and binned over 1 nm. Solid lines are the fits to each trace for 2 exponential rises and 1 exponential decay. The averages and standard deviations are reported in the main text.

$$S = \Sigma_{i=0}^{n} A_i * (1 - e^{-k_i t}) \tag{10}$$

S is the signal of the CdSe or ZnO, A_i is the amplitude of the exponential component i, with time constant k_i. The instrument response is taken into account by convoluting the exponential traces with a gaussian and multiplying with a step function. The fittings utilized the Nonlinear Least Squares method to minimize χ^2, employing the lmfit python package. Each trace was weighted with the standard deviation at each point. To correctly fit the overall shape in the UV, a single exponential decay was included alongside the exponential rises to account for the decrease in the signal after 1 ns. Time zero also cannot be accurately fit since the signal begins from 0, thus this parameter was held constant. The standard deviation of the fitted parameters was then calculated as the variation in the parameter needed to change χ^2 by 1. To make an objective decision on the correct number of components to use, the full set of kinetic traces for each material were fit sequentially to a greater number of exponentials (up to 3) while computing the Akaike and Bayesian Information Criterion (AIC and BIC, respectively), as defined in section S5.[13]

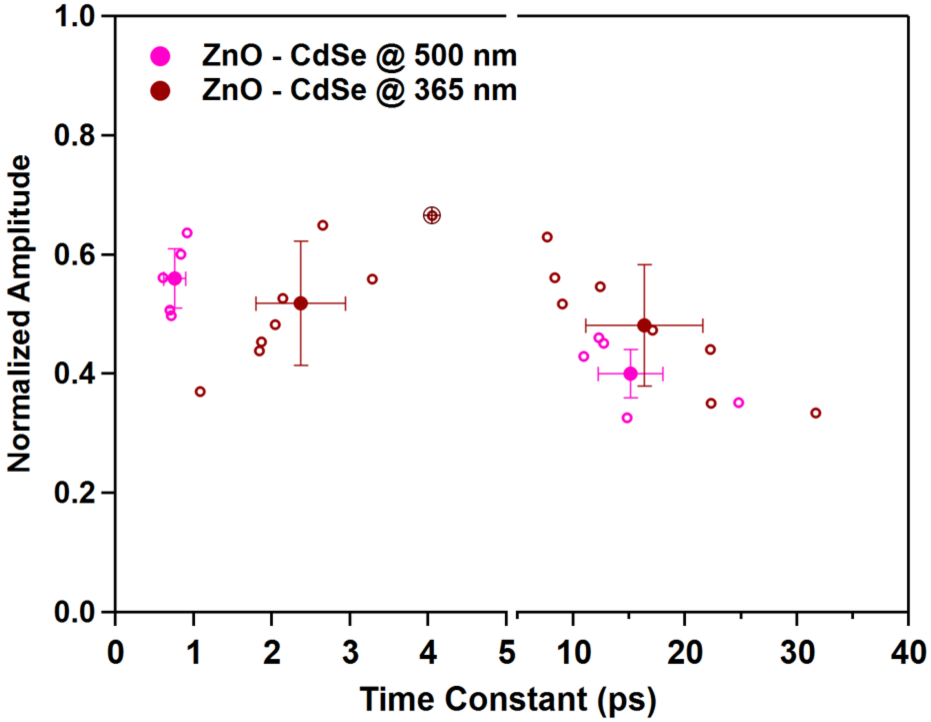

Figure 11: Individual and average time constants for the first two components of the kinetic fittings. Open circles represent the kinetic fittings of individual spot datasets, while the solid circles are the average of the spot datasets, representing the kinetics of the half datasets. Pink points are the fit values for CdSe, at 500 nm, and dark red points are the kinetic fits for ZnO, at 365 nm.

8 Characterization

Figure 13 shows typical SEM images of ZnO nanorods, after sensitization. To avoid artifacts related to charging, the nanorods were coated with 5 nm of platinum prior to imaging. All images were acquired on a Hitachi 4800 with a working distance of 5.6 mm, in ultrahigh resolution mode. The accelerating voltage was 1 keV. The 2.6 nm quantum dots are not visible due to the platinum coating and low estimated quantum dot coverage. Charging effects prevent quality high resolution images of uncoated samples. The nanorods were sized by taking a survey of the SEM images, the histogram for these are shown in figure 14. The measured length of the nanorods must be corrected by approximating the tilt of the nanorods from the surface normal at 50 °. The length of the nanorods is then 380 ± 60nm with a 60 ± 10nm width.

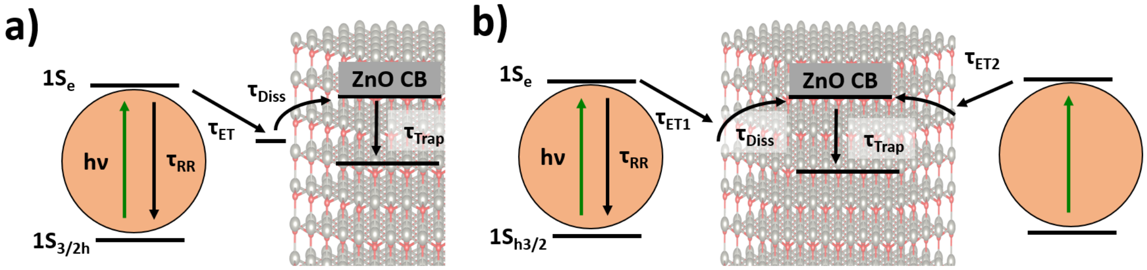

Figure 12: a) A graphic illustration of the 3-state model as it was implemented during global fitting, and described by equation 13. b) A graphic illustration of 4-state model as it was implemented during global fitting, and described by equation 14.

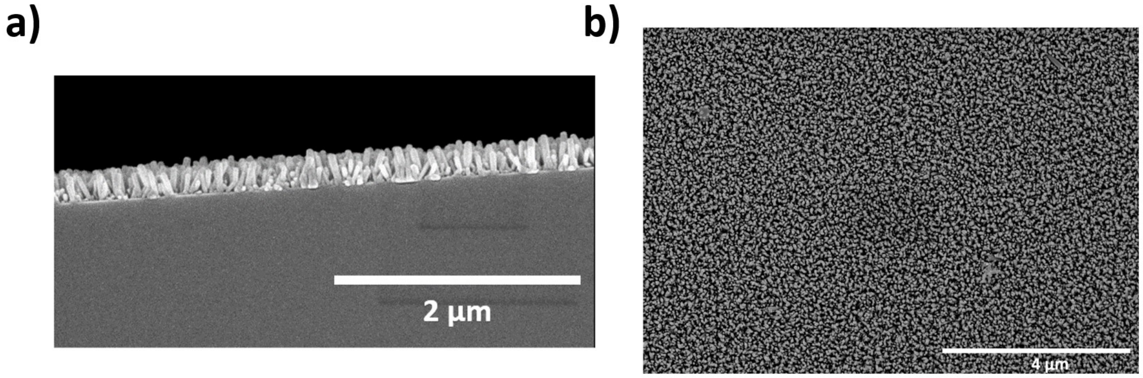

Figure 13: a) Cutaway view of sensitized ZnO nanorods, prepared by sputter coating with 5 nm of platinum. b) Wide view SEM image used to estimate the density of ZnO nanorods.

Figure 15a shows the X-ray diffraction spectrum for randomly oriented, and oriented nanorods of ZnO. The c-axis oriented nanorods have a prominent peak for the [0 0 2] reflection with low intensity of the [1 0 0] and [1 0 1] reflections. Randomly oriented nanorods have similar intensities for all three planes. The band gap of ZnO nanorods was estimated by Tauc fitting for a direct band gap semiconductor to be 3.26 eV, as shown in figure 15b.

Material	τ_1	τ_2	τ_{RR}	τ_{trap}
2.3 nm CdSe - ZnO				
CdSe	1.0 ± 0.2 ps (50 ± 4%)	25 ± 8 ps (37 ± 4%)	1e6 *ps* (13%)	—
ZnO	0.9 ± 0.1 ps (60 ± 5%)	14 ± 5 ps (40 ± 5%)	—	—
2.6 nm CdSe - ZnO[a]				
CdSe	0.8 ± 0.2 ps (56 ± 4%)	15 ± 3 ps (40 ± 4%)	7.9 *ps* (5 ± 1%)	—
ZnO	1.8 ± 0.3 ps (48 ± 9%)	13 ± 3 ps (52 ± 8%)	—	17 ± 1 ns (−100%)
2.6 nm CdSe - Annealed ZnO				
CdSe	2.5 ± 0.6 ps (43 ± 5%)	53 ± 11 ps (48 ± 3%)	7.9 *ps* (8 ± 6%)	—
ZnO	3.4 ± 0.5 ps (41 ± 4%)	47 ± 6 ps (59 ± 3%)	—	21 ± 2 ns (−100%)
4.2 nm CdSe - ZnO				
CdSe	1.5 ± 0.3 ps (38 ± 3%)	70 ± 10 ps (38 ± 3%)	1e6 ps (24%)	—
ZnO	4.3 ± 0.5 ps (47 ± 4%)	77 ± 11 ps (53 ± 4%)	—	—

Table 1: Time constants obtained via sum-of-exponentials fitting. Excitation wavelengths were 590 nm, 515 nm, and 485 nm for the 4.2 nm CdSe, 2.6 nm CdSe, and 2.3 nm CdSe respectively. All samples had target target <N> of 0.2. All traces in the UV were collected at 365 nm, and the visible traces were collected at 470 nm, 500 nm, 495 nm, and 590 nm, for the 2.3 nm CdSe, 2.6 nm CdSe, 2.6 nm CdSe@A-ZnO and 4.2 nm CdSe. In parentheses are the amplitudes of each exponential component.

$$\begin{aligned}
Actual\ QDs\ nm^{-2} &= \frac{\Delta A * N_A}{\epsilon_{CdSe} * \rho_{ZnO} * SA_{ZnO}} \\
Ideal\ QDs\ nm^{-2} &= \frac{0.835}{D^2_{CdSe}} \\
\%\ Monolayer &= \frac{Actual}{Ideal} * 100
\end{aligned} \tag{11}$$

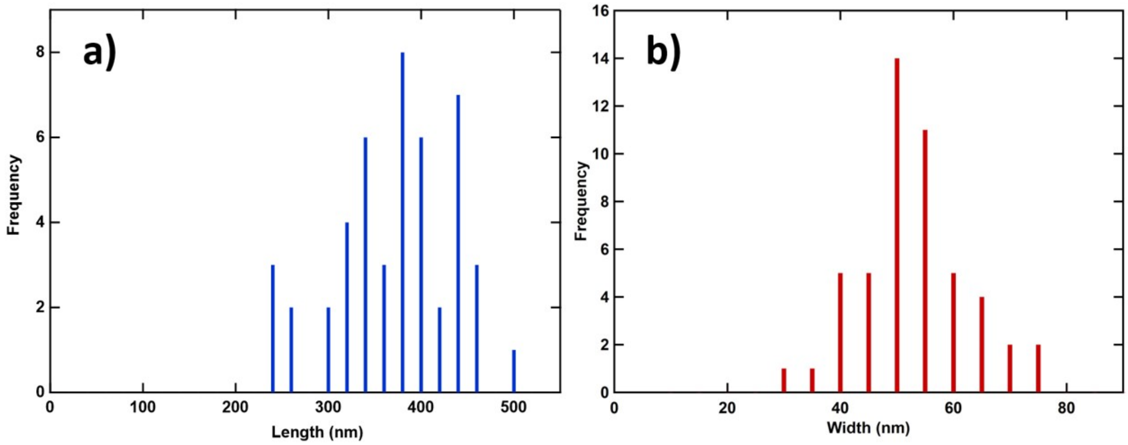

Figure 14: Size histograms of ZnO nanorods obtained from a survey of SEM images for the a) length and b) width. The length of the nanorods was corrected by accounting for a 50 degree average tilt of the nanorods from the surface normal. The average length is 380 nm and the average width is 55 nm.

Equation 11 shows the calculation of the quantum dot coverage on the ZnO surface. The actual density of QDs per square nm uses the absorption difference at the first excitonic peak (ΔA) divided by the molar absorptivity (ϵ_{CdSe}) and multiplied by Avogadro's number to give the number of quantum dots, which is over a square centimeter. This value is then divided by the total surface area by taking the nanorod density per square micrometer (ρ_{ZnO}) multiplied by the average surface area of a nanorod (SA_{ZnO}). The ideal value is obtained by dividing a prefactor by the given quantum dot diameter squared (D_{CdSe}^2). The prefactor includes the constants for the calculation of surface area required for close packed spheres. Thus, the percent monolayer is obtained by taking the actual QDs per square nanometer divided by the ideal times 100. The resulting coverage is found to be 8% and 12% for CdSe@ZnO and CdSe@A-ZnO respectively.

Transmission electron microscopy (TEM) was performed on a JEOL 2100 Cryo-TEM, with an accelerating voltage of 200 keV. The ZnO nanorods were scraped off a synthesized sample and deposited on a copper grid (purchased from Ted Pella). Typical nanorods are shown in figure 16. Terraces can be seen along the length of the nanorods, which are characteristic of the $[1\,0\,\bar{1}\,0]$ facets.[14] Since the hydrothermal growth results in well faceted nanorods, the pointed termination is where the nanorod

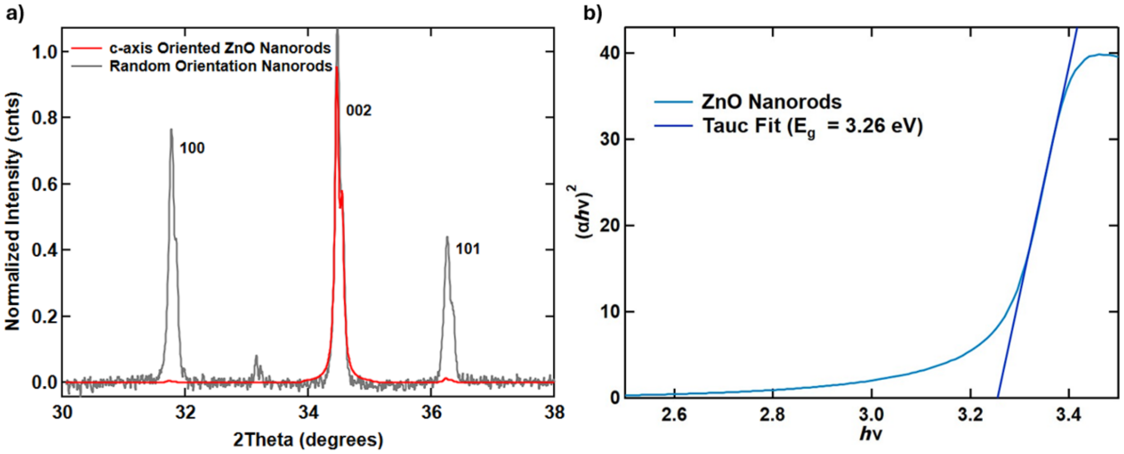

Figure 15: a) Comparative X-ray diffraction measurements of c-axis oriented wurtzite ZnO nanorods (red trace) vs. randomly oriented nanorods (gray trace). Three distinct crystal planes can be found, with [1 0 0] at 31.8 degrees, [0 0 2] at 34.5 degrees, and [1 0 1] at 36.3 degrees. b) Tauc plot for ZnO nanorods for a direct band gap semiconductor, along with a fit to the linear region. The intercept with the x-axis is the estimated band gap, 3.26 eV.

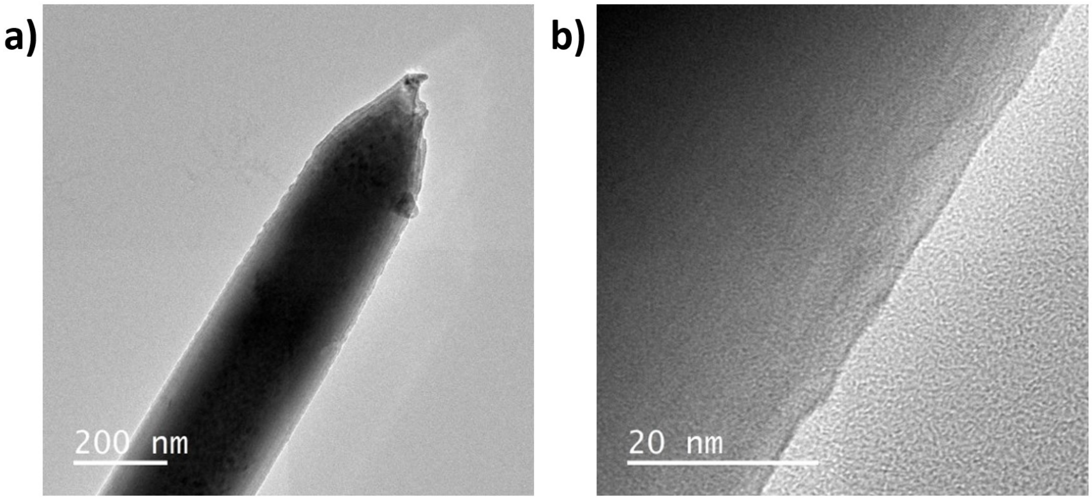

Figure 16: a) TEM of typical unsensitized ZnO nanorods are shown, with a width of 220 nm. b) The faceted $[1\,0\,\bar{1}\,0]$ sides are not well resolved. However, terraces can be seen, which are due to the rough surface morphology of the $[1\,0\,\bar{1}\,0]$ facet.

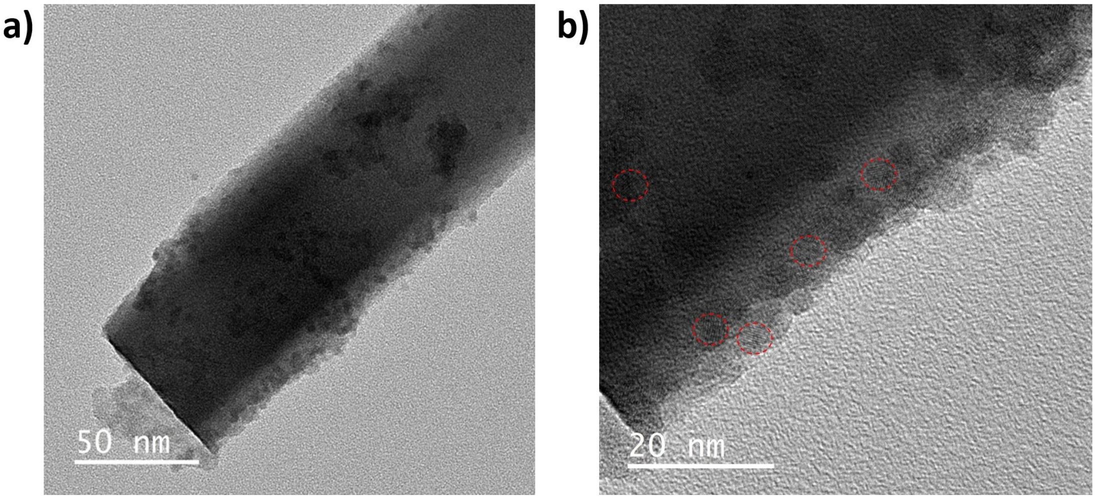

Figure 17: a) TEM of a sensitized ZnO nanorod. The sensitized quantum dots are predominantly located near the terminating end of the nanorod (within 200 nm). b) Closeup of the edge of the nanorod, with individual, well resolved quantum dots highlighted with dotted red circles.

broke off from the substrate surface, which includes a portion of the ZnO seed layer.

ZnO nanorods sensitized with quantum dots are shown in figure 17. The quantum dots can be seen by high contrast areas on the surface of the nanorod. The high crystallinity of the QDs post-sensitization is evidenced by the visible diffraction fringes seen in the circled areas of figure 17b.

As shown in figure 18, annealing at 400 C under vacuum caused a red shift of the band gap. As reported in reference [15], the band bending at the $[1\,0\,\bar{1}\,0]$ surface reached a magnitude of -0.79 eV through hydroxide adsorption, which is large enough to induce metallic character near the surface. Since the conduction band is expected to lie approximately 350 meV above the Fermi level, the removal of this band bending would red shift the apparent band edge. The penetration depth of the band bending as great as 6 nm, which would subject approximately 36% of the ZnO volume to band bending since the nanorods are about 60 nm wide. Complementary to this, the photoluminescence spectrum shows a similar red shift and narrowing of the emission spectra, both near the band gap and in the redder region. The narrower emission spectrum indicates that the structure of the ZnO surface is relaxed in a significant, non-reversible way since the static UV-Vis of the ZnO does not recover after sensiti-

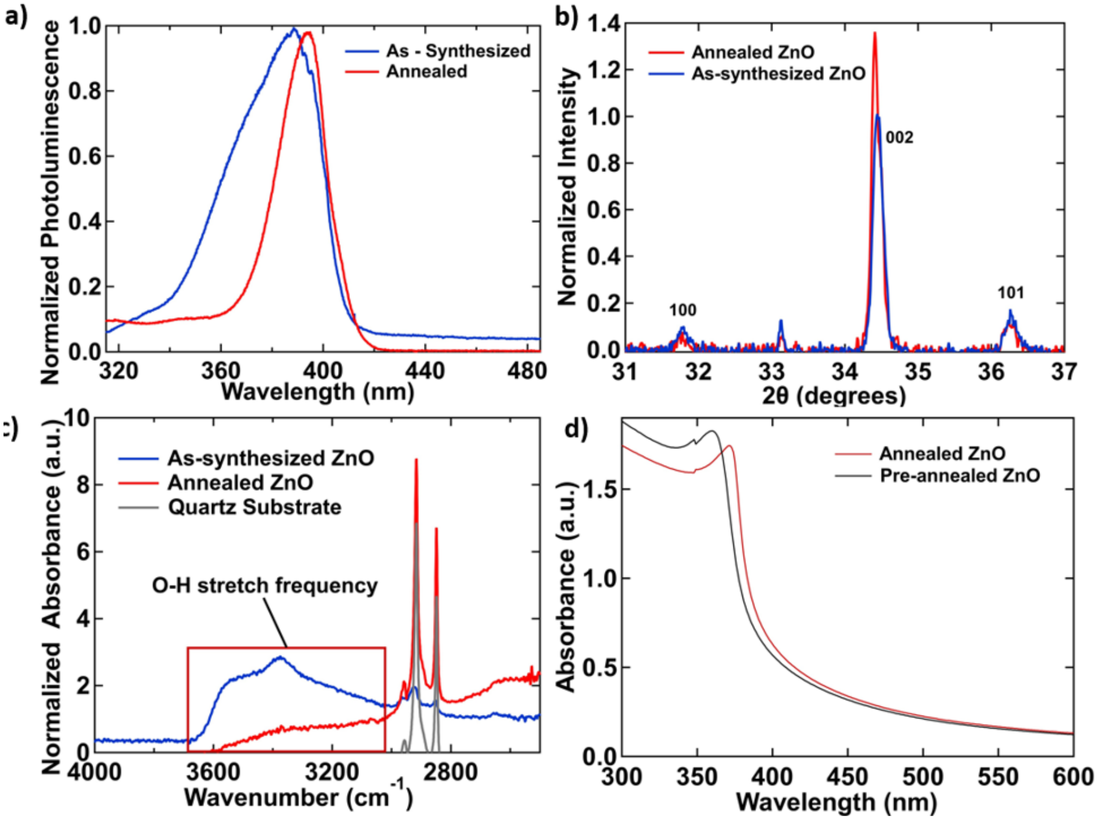

Figure 18: a) Photoluminescence of a sensitized ZnO nanorod. The sensitized quantum dots are predominantly located near the terminating end of the nanorod (within 200 nm). b) Closeup of the edge of the nanorod, with individual, well resolved quantum dots highlighted with dotted red circles.

zation with CdSe in methanol. The reduced emission below the band gap indicates a lower defect density compared to pre-annealing, even while the Urbach tail of the UV-Vis indicates similar levels of amorphicity before and after annealing.[16] Within the XRD spectrum, only the [0 0 2] reflection has significant intensity due to the preferential orientation of the nanorods, with the c-axis normal to the quartz substrate. Annealing results in a shift of this reflection by 0.15 degrees to smaller angles and a narrowing of the peak, which corresponds to a lengthening of the nanorods along the c-axis. This change could reflect reduced strain in the nanorods due to the epitaxial growth on the quartz substrate. Since ZnO is a piezo-electric material, strain induces a static electric field within the nanorods. If pre-annealed samples are strained,

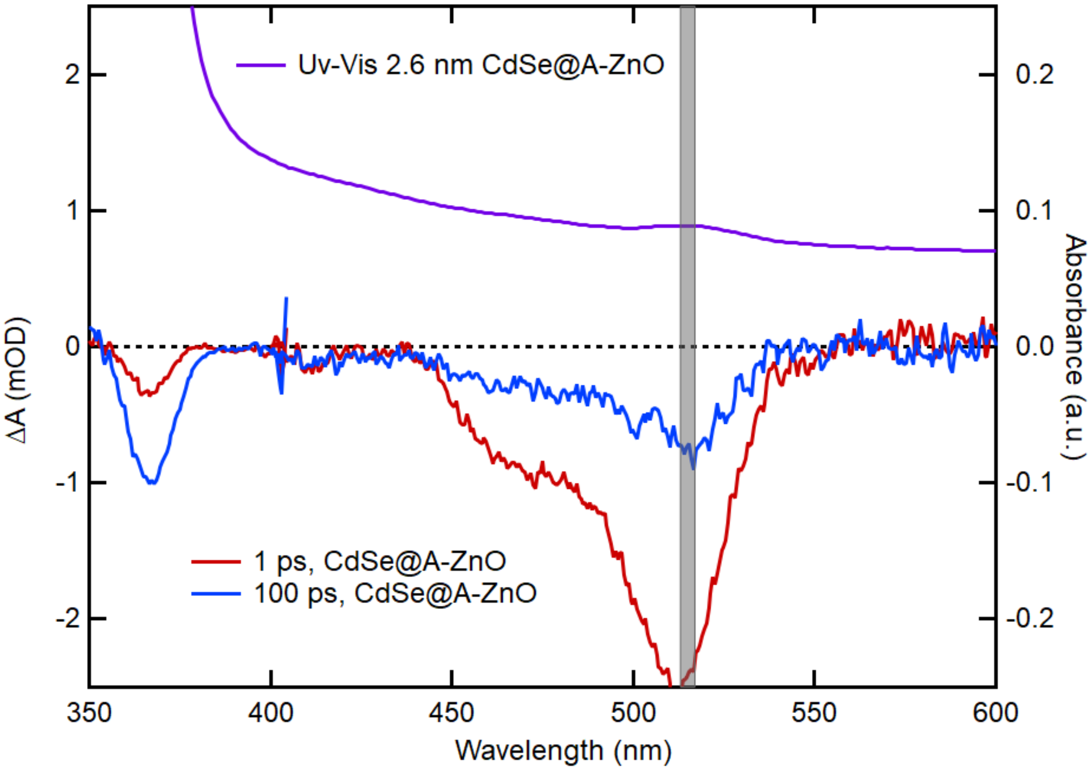

Figure 19: Transient absorption spectra of 2.6 nm CdSe@A-ZnO at 1 ps, CdSe-sensitized ZnO (CdSe@ZnO) nanorods at 1 ps (red), and at 100 ps (blue) after photoexcitation (all left axis). The spectral bandwidth of the pump light is highlighted with the gray box, centered at 513 nm with 4 nm FWHM. Also shown are the corresponding static UV/visible absorption spectra of CdSe@A-ZnO nanorods (purple).

this field could also have lead to a static dipole moment across the ZnO nanorods. However, it's unlikely that such an effect could produce the scale of results seen here.

Figure 19 shows spectral traces for an example dataset of 2.6 nm CdSe@A-ZnO compared to the static Uv-Vis spectrum. The spectra are taken at 1 ps and 100 ps from figure 2D. The 1 ps trace (red) shows a strong bleach centered at the 2.6 nm CdSe first excitonic transition, with a shoulder at approximately 470 nm corresponding to the second excitonic transition. After 100 ps, spectral weight has transferred from the visible to the UV, corresponding to the ZnO excitonic transition, at 365 nm.

XPS measurements were performed with a Kratos Axis Ultra X-ray photoelectron spectrometer with monochromatic 210 W Al $K\alpha$ excitation (14 kV, 15 mA). The spectra were processed with the Casa XPS software. The carbon 1s photoemission peak at a binding energy reveals a low concentration of adsorbed organic molecules. This shows that the organic compounds used as surfactant molecules or in the metal oxide precursors during the synthesis remain at the nanorod surface in some low concentration. The two peaks in the O 1s photoemission are usually assigned to surface oxygens (hydroxyls) and bulk-like oxygens with comparable intensities due to the surface sensitivity of XPS. Oxygen defects within the bulk provide a third peak at higher binding energies, which is observed in the low growth time samples. A simple linear background subtraction was applied at the Zn 3d edge, and a U 2 Tougaard background was applied at the O 1s edge.[17] The fitted parameters are listed in table 3 and 2.

Fitted Zn 3d XPS parameters				
Material	$E1_{center}$ (FWHM)	E1 Area	$E2_{center}$ (FWHM)	E2 Area
Unannealed ZnO	9.46 eV (1.13 eV)	230.8	10.11 eV (1.56 eV)	766.5
Annealed ZnO	9.56 eV (1.39 eV)	734.3	10.18 eV (1.66 eV)	540.8

Table 2: Fitted XPS parameters for the Zn 3d for both annealed and unannealed samples.

Fitted O 1s XPS parameters						
Material	$E1_{center}$ (FWHM)	E1 Area	$E2_{center}$ (FWHM)	E2 Area	$E3_{center}$ (FWHM)	E3 area
Unannealed ZnO	530.78 eV (1.19 eV)	2084.4 eV	532.17 eV (1.927 eV)	2084.4	532.8 eV (3.88 eV)	1845 eV
Annealed ZnO	530.66 eV (1.264 eV)	3215.5 eV	532.20 eV (2.11 eV)	3212.5	533.9 eV (3.36 eV)	451.8 eV

Table 3: Fitted XPS parameters for O 1s for both annealed and unannealed samples.

The C 1s photoelectron peak was used to calibrate the energy of the O 1s and

Zn 3d measurements, which are shown in the main text. At the oxygen 1s peak, the signal can be fit to a sum of three Gaussian functions, which are attributed to oxygen defects, adsorbed hydroxides, and lattice bound oxygen.[18] Oxygen defects are not always observed in these samples when grown for longer times. The contribution of defect states and hydroxide species to the signal decreases after annealing, matching the reduction in organic contaminants. The Zn 3d peak could be adequately fit with a sum of two Gaussian functions, which could represent the different exposed facets. A single, skewed Gaussian could not account for the shape of the signal. The peak position and contribution of each fitted component is shown in table S2 for the Zn 3d measurements, and table S3 for the O 1s measurements. The Zn 3d character shows a shift of $\sim$120 meV to lower binding energies after annealing, along with a narrowing of the FWHM by 70 meV. A corresponding shift of the O 1s peak by 150 meV to lower binding energies is also seen. As has been interpreted in references [15, 19], the reduced elemental carbon percentage and peak shifts and narrowing are attributed to a reduction in the downward band bending of the valence and conduction bands near the surface as a result of a removal of surface adsorbates.

The static UV-Vis spectra ZnO after sensitization with different QD sizes is shown in figure 20, along with the spectra of the native oleic acid coated 2.6 nm CdSe compared to the MPA coated, phase-transferred CdSe. The QDs show no change in absorption spectrum during the ligand exchange and phase transfer aside from a slight solvatochromatic shift due to a change in the dielectric constant from toluene with an oleic acid coating, to methanol and coated with MPA.[20] The sensitized ZnO features a small peak at the CdSe excitonic transitions (590, 515, and 485 nm) and a sharp absorption onset at the ZnO band gap of 3.3 eV, along with an extended tail below the ZnO band gap from crystalline disorder forming subbandgap states.[21, 22] Despite this extended tail, there is no evidence of single photon absorption at the ZnO band gap in transient experiments. The absorption difference between the unsensitized and sensitized ZnO at the CdSe excitonic peak was used to calculate the concentration of CdSe adsorbed to the ZnO. Using the estimated QD concentration, the QD coverage is estimated at 8.8 and 42 % of a monolayer for the 2.3 nm and 4.2 nm CdSe respectively.

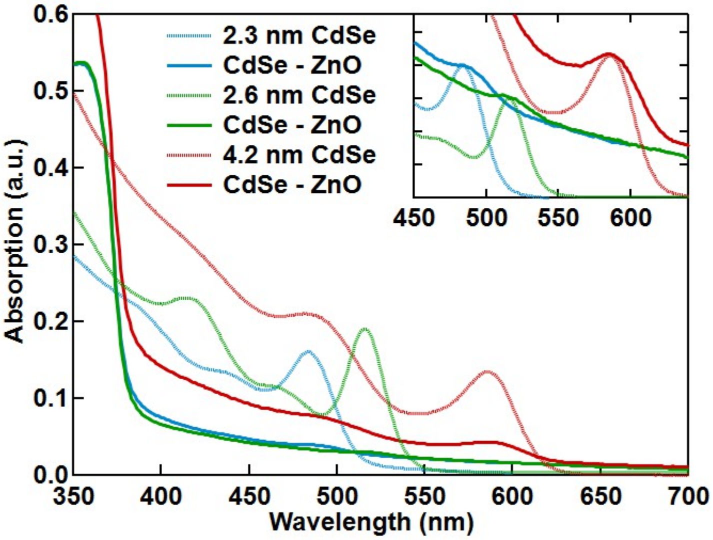

Figure 20: The static Uv-Vis spectrum of three conjugated CdSe - ZnO samples is shown (solid lines), along with solution phase static UV-Vis after phase transfer (dotted lines). The first excitonic transition is at 485 nm, 515 nm, and 590 nm corresponds to quantum dots of size 2.3 nm (blue), 2.6 nm (green), 4.2 nm (red) quantum dots. Also shown is 2.6 nm CdSe in toluene coated with oleic acid (light green).

9 Two Photon Absorption in ZnO

Two photon absorption in ZnO was measured using the same 515 nm pump as the sensitized sample. The low dimensionality of ZnO increases the magnitude of the electric field, allowing for a low threshold for two photon absorption.[23] Datasets were measured for fluences spanning an order of magnitude, including at the fluence matching the sensitized sample, which is shown in figure 21. An excited state absorption appears at 380 nm within the first few 100's of fs due to band gap renormalization (BGR), which disappears as the carriers rapidly thermalize to the band edge. At the same time, a high magnitude bleach appears and relaxes within the first 0.2 ps, which could be due to a two-photon enhanced self-phase modulation from the intense electric field.[24, 25] BGR resolves as the electrons and holes cool to the band edge and condense into excitons, resulting in a bleach due to phase-space filling centered at 365 nm and decaying with multiexponential character. At the fluence used in charge transfer experiments, the amplitude of the TPA bleach is approximately -100 μOD at

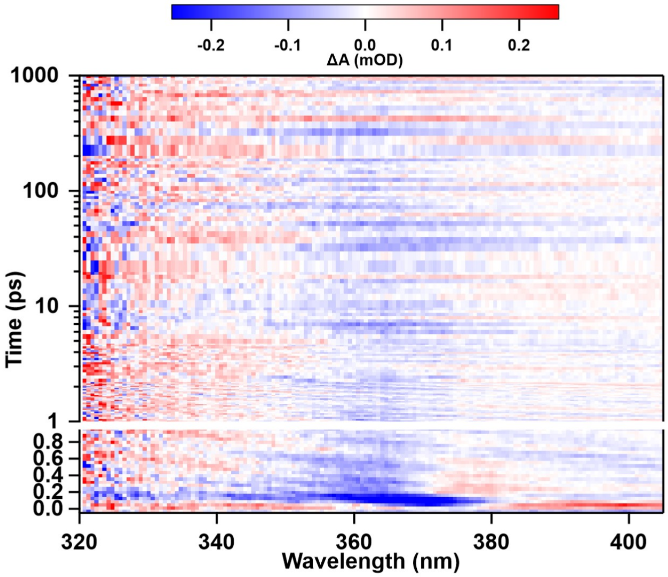

Figure 21: 2D dataset of two photon absorption in bare ZnO at the target fluence of 72 μJ/cm^2.

300 fs after t0, while in the charge transfer experiments the amplitude at 300 fs is -15 μOD. This indicates TPA is approximately 7x less in sensitized samples, at the same fluence. Potentially, absorption from the CdSe quantum dots reduce the amplitude of the electric field enough to lower the total TPA in sensitized experiments.

10 Dye Sensitized ZnO

The optical characteristics of the CTS is illustrated by measurements on dye-sensitized ZnO, which do not show a UV transient signal from the rapidly populated (<300 fs) intermediate state. Dye sensitized ZnO was measured for a comparison to literature, and CdSe sensitized samples. 532 nm pump excites the ^{1}MLCT of N719, which relaxes to the ^{3}MLCT state which persists for 20 ns.[26] The spectral comparison is shown in figure 22a between N719 sensitized ZnO and N719 dye in ethanol. The N719 dye shows a broad ESA from 400 nm to 320 nm, followed by a bleach at 310 nm of the ligand-centered state.[27] The sensitized ZnO shows a strong bleach at 370 nm due to phase space filling of photoinjected electrons, coupled with an induced absorption at 350 nm due to an increased refractive index of the free conduction band carriers,

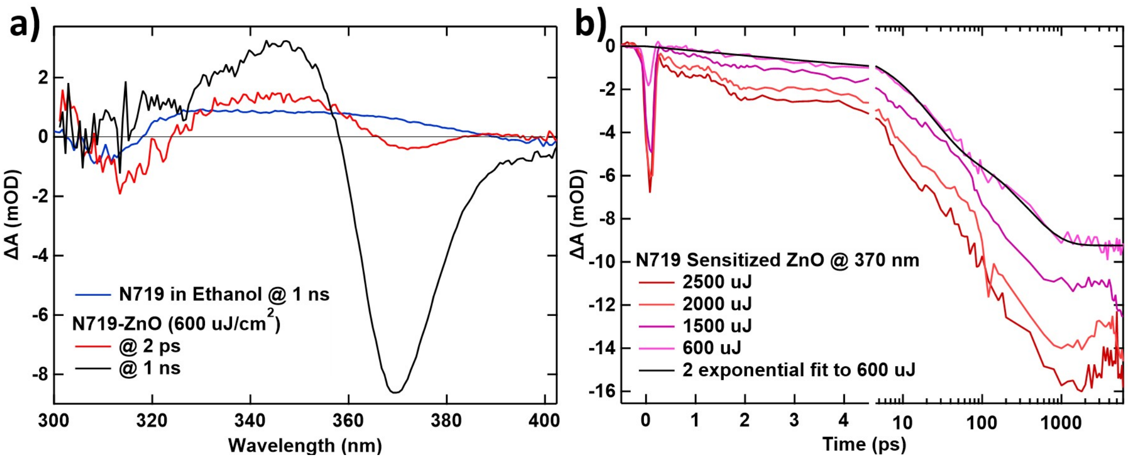

Figure 22: a) spectral slices at 2 ps (red trace) and 1 ns (blue trace) for N719 sensitized ZnO nanorods after excitation at 532 nm with 600 600μJ/cm^2, along with a representative spectral trace from N719 in ethanol at 1 ns (blue trace). b) Kinetic traces at 370 nm in N719 sensitized ZnO after excitation with fluences from 600 - 2500 μJ/cm^2, along with a biexponential fit to the 600 μJ/cm^2 (blue trace).

which also contributes to a bleach at wavelengths above the band edge exciton due to a decreased refractive index below the band edge.[22]

Figure 22b shows kinetic traces at 370 nm for 4 excitation fluences. The rising signal requires a biexponential function to be satisfactorily fit. The time constants are 22 ± 2 ps and 380 ± 50 ps, with amplitudes of 49 and 51 % respectively, similar to literature.[19, 27, 28] N719 transfers an electron from the photoexcited MLCT into the intermediate ICT state within 600 fs, followed by dissociation into the bulk DOS.[19, 27–29] The injection yield is linear with fluence, along with an increased baseline due to two-photon injection.

Within the context of CdSe sensitized ZnO, a bound interfacial state should not contribute to a bleach of the band edge transition in ZnO due to the electron not occupying the bulk DOS. CTSs are likely formed from subbandgap surface states in ZnO.[28, 30, 31] Dipole allowed transitions to CTSs have an energy equal to the difference between the hole state left in the QD valence band and the electron acceptor state in ZnO, minus the Coulombic attraction between them.[14, 32–34] Given an approximate driving force of $\sim$ 0.11 eV and an optical QD band gap of 2.41 eV, an optical transition to the CTS would be <2.3 eV depending on the magnitude of

Coulombic attraction (∼ 300 meV),[35] and should not complicate the UV kinetics. The insensitivity of the UV probe to CTSs is illustrated by measurements on dye-sensitized ZnO, which do not show a UV transient signal from the rapidly populated (<300 fs) intermediate state.

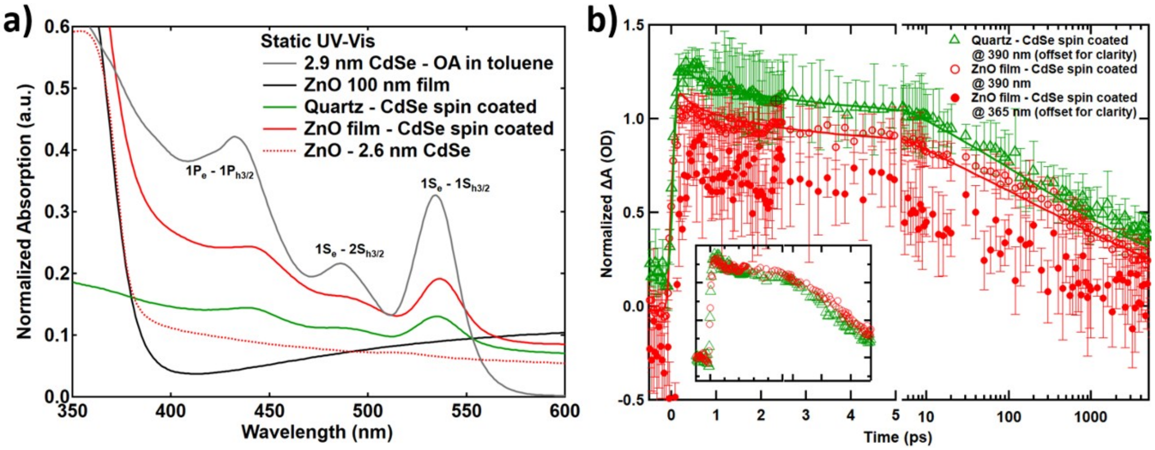

Figure 23: a) Static Uv-vis spectrum of 2.6 nm CdSe in solution (gray line for oleic acid capped quantum dots in hexane). Also shown is the the ZnO film prior to sensitization (black), and the ZnO film spin - coated with 2.9 nm CdSe (red solid line). Also shown for reference are ZnO nanorods chemically conjugatad with CdSe (red dotted line, reproduced from Fig. 1) and CdSe spin coated onto a quartz substrate (green). b) Representative transient kinetic traces for the spin - coated ZnO sample is shown at 390 nm (open red circles) and at 365 nm (closed red circles, offset for clarity). The spin - coated quartz control sample is also shown at 390 nm (green open triangles, offset for clarity). The data at 390 nm was fit with stretched exponentials, as detailed in the text (solid lines). The inset shows the kinetic data points at 390 nm without any offset and without the kinetic fits for direct comparison. Both spin coated samples had target <N> of 0.8.

11 Spin Coated CdSe

A sensitized ZnO sample was prepared with an alternative procedure in order to attempt a study of a single crystal surface while enforcing a high concentration of CdSe. This procedure uses a solid state ligand exchange as is common in the preparation of

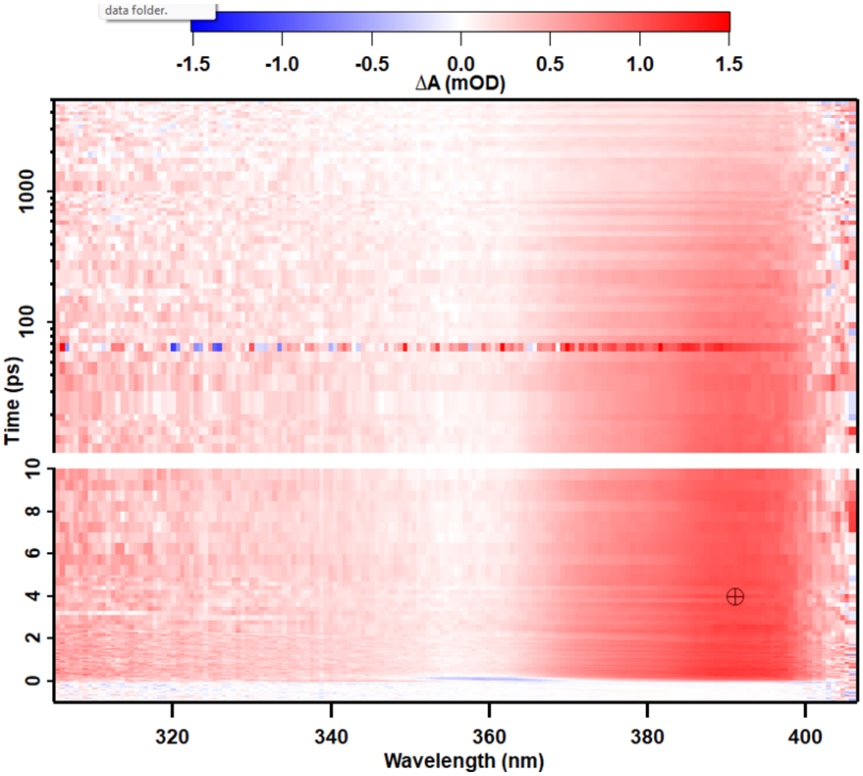

Figure 24: A 2D dataset for the 2.9 nm CdSe spin-coated ZnO sample. The target excitation was <N> of 0.8, at 533 nm.

devices.[36] A solution of CdSe QDs coated with oleic acid was spin coated onto a 100 nm thick ZnO single crystal, grown with pulsed laser deposition. A 1% v/v solution of MPA in acetonitrile was deposited on top and allowed to react for 5 minutes, then rinsed with acetonitrile. This was repeated 3 times to create a thick layer of CdSe. Figure 23a shows the static UV-Vis spectrum of this sample alongside the chemically conjugated sample. Comparing the dotted and solid red traces for the chemically conjugated and spin coated samples respectively illustrates the high concentration of CdSe compared to the solution phase sensitization. Due to the higher concentration, a higher fluence of 512 μJ/cm^2 was used. The mean excitonic state is higher for these experiments, at 0.8. This higher excitation allows a QD based UV-signal to be measured, which is necessary to confirm excitation of the QD's in the absence of charge injection.

Shown in figure 23b are the kinetics of the spin coated ZnO and quartz in red and green respectively. The kinetic traces for the CdSe was taken far from the bleach feature of ZnO, at 390 nm. This ESA likely originates from biexcitonic induced shifts of a high lying excitonic transition, as shown in figure 2 at 360 nm for 2.6 nm CdSe.[10] In the chemically conjugated samples this signal is too weak to observe and is blue shifted significantly. Here, the high coverage of CdSe allows a clear signal in the UV probe region, which overlaps with an expected ZnO signal at 365 nm. A decay on the multi-nanosecond timescale is observed for both samples, with identical kinetics measured at 390 nm. In solid red circles is shown the kinetics of the spin coated ZnO at 365 nm. With charge injection, the spectral bleach of PSF would lead to complex dynamics at this wavelength. Instead, the kinetics match the CdSe exactly as shown in the normalized kinetic traces. The inset contains the kinetics at 390 nm without an offset for direct comparison of the CdSe kinetics, which are nearly identical. Figure 24 shows the 2D dataset for the spin coated ZnO. The ESA is inhomogeneously broadened and extends to approximately 360 nm on the blue side and 400 nm on the red. A bleach at 365 nm due to PSF would strongly distort the shape of the ESA, but this is not observed.

The equivalent dynamics between all kinetic traces for ZnO and quartz spin coated samples, and the absence of a spectral PSF feature at 365 nm, indicates that there is no charge injection. This sample is illustrative of the dynamics of a sample with the same surface chemistry as a sensitized sample, but without any electronic coupling and likely a large degree of inter-quantum dot dynamics. This trace can be fit best to a stretched exponential with an exponential factor of 0.21, and time constant of 380 ±60 ps. The traditional approach to estimating the timescale of charge injection is to use the difference in time constants from a sample such as this, with similar surface chemistry but no charge injection, and the sensitized sample discussed in the main text, as shown in equation 12:

$$1/\tau_{ET} = \frac{1}{\tau_{CdSe-ZnO}} - \frac{1}{\tau_{CdSe-Control}} \tag{12}$$

Applying formula 12 with the first CdSe decay constant gives a ET time of 1.1 ps. However, this is unnecessary in this case since the movement of photoexcited carriers can be accurately tracked from their departure in CdSe to their arrival in ZnO. The spin coated sample is a good example of the effects of aggregation and poor ligand exchange. Since the oleic acid could not be completely removed in this approach and no charge injection was measured, the observed dynamics are purely that of oxidation or trapping of carriers. However the stretched exponential function does not give a physical measure of the actual time constant distribution.[12] The stretched exponential was applied to the UV and visible datasets, but did not provide a better fit than a multi-exponential model.

12 Global Target Analysis

To extract the most accurate time constants and physical picture, holistic kinetic models were applied to the full datasets for each sample to fit all spot datasets in the UV and visible, simultaneously. The two models considered the most plausible are shown pictorially in figure 12a and equation 13, and 12b and equation 14, referred to as the three and four state models respectively. Figure 12a considers a single QD population with a single charge injection rate, while figure 12b considers two distinct QD populations with two injection rates and an intermediate state only for the fast charge injection pathway. Alternative permutations give poor agreement with experimental data. During fitting the time constants were shared across the whole dataset (visible + UV) while amplitudes were shared across half-datasets (visible and UV half-datasets have distinct amplitudes).

$$
\begin{aligned}
dN_{QD} &= -k_1 * N_{QD} - k_{rr} * N_{QD} \\
dN_{CTS} &= k_1 * N_{QD} - k_{diss} * N_{CTS} \\
dN_{ZnO} &= k_{diss} * N_{CTS} - k_{trap} * N_{ZnO}
\end{aligned} \tag{13}
$$

$\mathrm{N_{QD}}$, $\mathrm{N_{CTS}}$, and $\mathrm{N_{ZnO}}$ are the electron population of the QDs, CTS, and ZnO respectively, where $N_{QD} = 1$ at t_0. k_{ET} is the rate constant for charge transfer from CdSe into the CTS, and k_{diss} is the rate constant for charge separation at the interface of CdSe and ZnO. k_{trap} is the rate of electron trapping, or back electron transfer, in ZnO. The standard differential equations in 13 were solved analytically and used to fit the relevant UV and visible datasets.

$$
\begin{aligned}
dN_{QD1} &= -k_1 * N_{QD1} \\
dN_{QD2} &= -k_2 * N_{QD2} \\
dN_{QD} &= dN_{QD1} + dN_{QD2} - k_{rr} * N_{QD} \\
dN_{CTS} &= k_1 * N_{QD1} - k_{diss} * N_{CTS} \\
dN_{ZnO} &= k_{diss} * N_{CTS} + k_2 * N_{QD2} - k_{trap} * N_{ZnO}
\end{aligned} \tag{14}
$$

N_{QD1} and N_{QD2} are the populations of excited QD-bound electrons that are attached to ZnO surfaces of different character. N_{QD} represents the sum of the two subpopulations of QDs that describes the total QD visible signal. The former population will experience a larger driving force, and thus undergo injection quickly, but may experience a potential at the surface that will force localization close to the surface. N_{QD2} represents the population of quantum dots that are not coupled to a strong downward surface potential, but may be electronically coupled to states with a lesser magnitude of downward bending, or even upward bending. The time constants k_1 and k_2 represent the rates of charge injection into the $[1\,0\,\bar{1}\,0]$ and $[0\,0\,0\,1]$ facets respectively. k_{diss} represents the rate of dissociation out of the potential well. Any intermediate state for the k_2 pathway is likely to be unobservable due to overlapping kinetics. For example, if k_1 and k_2 are well separated in time, this would mean that k_2 is transferring electrons into a higher energy level with a fast dissociation into the bulk DOS. If k_{diss} was fast, then dissociation after k_2 would be much much faster. If k_{diss} is slow, then the timescales of k_1 plus dissociation would overlap with k_2 plus dissociation, and they would become inseparable. Within this framework, charge transfer into a CTS plus any dissociation out of that state is approximated with a single time constant. It should be noted that the amplitude of either charge injection pathway is dependent on the population of QDs bound to each crystal facet.

Heterogenous Injection (HI) is defined as charge transfer from indirectly attached QDs. These quantum dots are not chemically bound to the surface, and thus have a weaker electronic coupling. Rather, these QDs can transfer a charge to a directly attached QD, or transfer a charge through physical but not chemically bound contact. This model is defined simply with a three state parallel decay model:

$$\begin{aligned} dN_{QD1} &= -k_{ET} * N_{QD1} \\ dN_{QD2} &= -k_{SET} * N_{QD2} \\ dN_{ZnO} &= k_{ET} * N_{QD1} + k_{SET2} * N_{QD} - k_{trap} * N_{ZnO} \end{aligned} \tag{15}$$

Where N_{QD} and N_{ZnO} are the electron populations in the quantum dots and ZnO respectively. k_{ET} and k_{SET} are the time constants for the direct and indirect quantum dots respectively. This model has been applied alongside the CTS model as the other likely explanation for the rising ZnO signal in terahertz spectroscopy.[37, 38] Within this interpretation, the injection from indirectly attached quantum dots could range from 20 to 100 ps. Charge transfer from indirect quantum dots proceeds first through an adjacent quantum dot, and then into the metal oxide. Since electron transfer from the directly attached quantum dot should be much faster than carrier diffusion between quantum dots, the overall rate can be approximated as the rate of charge transfer between quantum dots. Injection from indirect quantum dots could be accentuated with exciton delocalizing ligands.[39, 40] Carrier diffusion between quantum dots is complicated by charge transfer taking place either into a neutral unexcited quantum dot, a neutral excited quantum dot, or a charged quantum dot post-electron transfer.

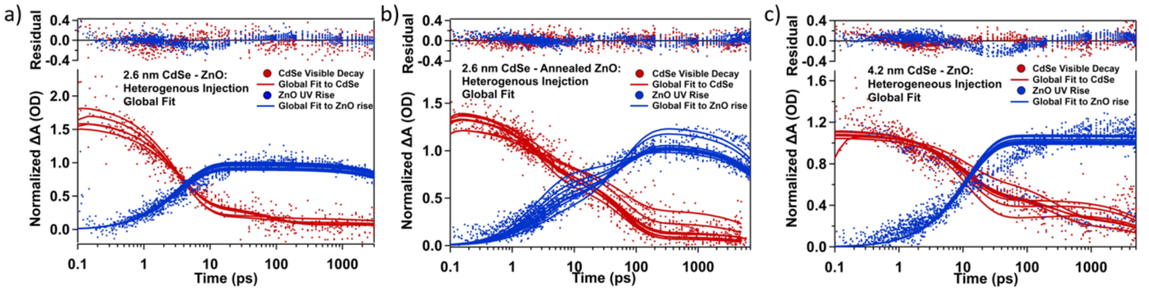

Figure 25: The global fits to the heterogeneous injection for a) 2.6 nm CdSe@ZnO, b) 2.6 nm CdSe@A-ZnO, and c) 4.2 nm CdSe@ZnO. Solid lines are the fits to the individual datasets. At top are the residuals for the global fits.

2.6 nm CdSe - ZnO 3-state Global Fit Results				
Material	τ_{ET1}	τ_{diss}	τ_{RR}	τ_{trap}
CdSe	3.76 ± 0.08 ps (90 ± 1%)	—-	$1e6$ ps (10 ± 0.4%)	—–
ZnO	—–	$0 \pm 0.03\%$ ps (100 ± 0.4%)	—–	$17 \pm$ 0.6 ns ($-100 \pm 1\%$)

Table 4: Time constants obtained via global fitting with a 3 state model to the measured kinetic traces at 365 nm for ZnO, and at 500 nm for 2.6 nm CdSe. In parentheses are the normalized amplitudes of each component.

Globally fitting the data to a 3-state model, which excludes HAS, is shown in figures 26 to 28, and included in table 4. The fitted traces show significant deviations to the experimental data, as seen in the residual data points. The 3-state model can also not reconcile the short time behavior of the visible/UV datasets, as seen by a τ_{diss} of 0 ps and the discrepancy between the visible data and fitted trace. At the same time, the UV data and fitted trace shows a large discrepancy between 3 and 100 ps. The overall oscillatory behavior of the residual data further shows that this model cannot accommodate the shape of the combined datasets.

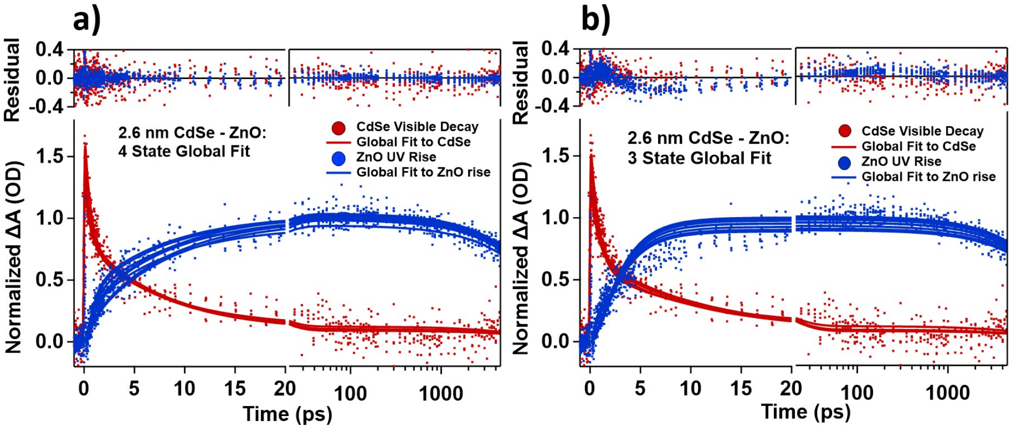

Figure 26: The a) 4 state and b) 3 state kinetic model fitted to 2.6 nm CdSe@ZnO. Red data points are kinetic traces in the visible probe region at 500 nm, representing CdSe kinetics. Blue data points are taken at 365 nm and represent the ZnO kinetics. Solid lines are the fits to the individual datasets. At top are the residuals for the global fits.

Sample	τ_{CdSe}	τ_{diss}	τ_2	τ_{RR}	τ_{trap}
2.6 nm CdSe - ZnO	$0.8 \pm 0.1\ ps$	$0.4 \pm 0.1\ ps$	$10 \pm 1\ ps$	$7.9 \pm 0\ ns$	$16 \pm 1\ ns$
2.6 nm CdSe - Annealed ZnO	$2.4 \pm 0.1\ ps$	$0.0 \pm 0.1\ ps$	$44 \pm 2\ ps$	$7.9 \pm 0\ ns$	$21 \pm 1\ ns$
4.2 nm CdSe - ZnO	$1.6 \pm 0.1\ ps$	$0.8 \pm 0.1\ ps$	$58 \pm 2\ ps$	$7.9 \pm 0\ ns$	—-

Table 5: Time constants obtained via global fitting to the measured kinetic traces at 365 nm for ZnO, and at 590 nm for 4.2 nm CdSe or 515 nm for 2.6 nm CdSe.

The kinetic models discussed above were used to fit 2.6 nm CdSe@ZnO, 2.6 nm CdSe@A-ZnO, and 4.2 nm CdSe@ZnO, as shown in figures 26 to 28. Each dataset includes the same wide scale sampling strategy as the 2.6 nm CdSe, where multiple spots were averaged and analyzed in parallel for both Visible and UV probes. For

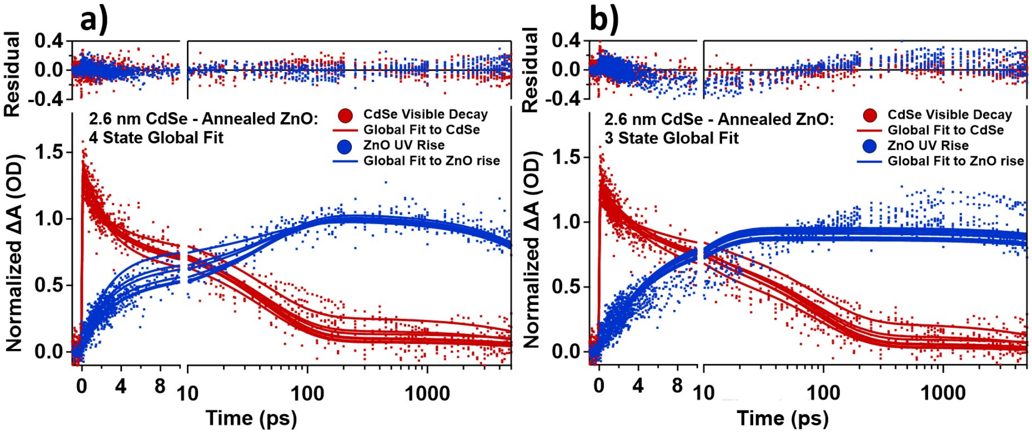

Figure 27: The a) 4 state and b) 3 state kinetic model applied to 2.6 nm CdSe@A-ZnO. Red data points are kinetic traces in the visible probe region at 495 nm, representing CdSe kinetics. Blue data points are taken at 365 nm and represent the ZnO kinetics. Solid lines are the fits to the individual datasets. At top are the residuals for the global fits.

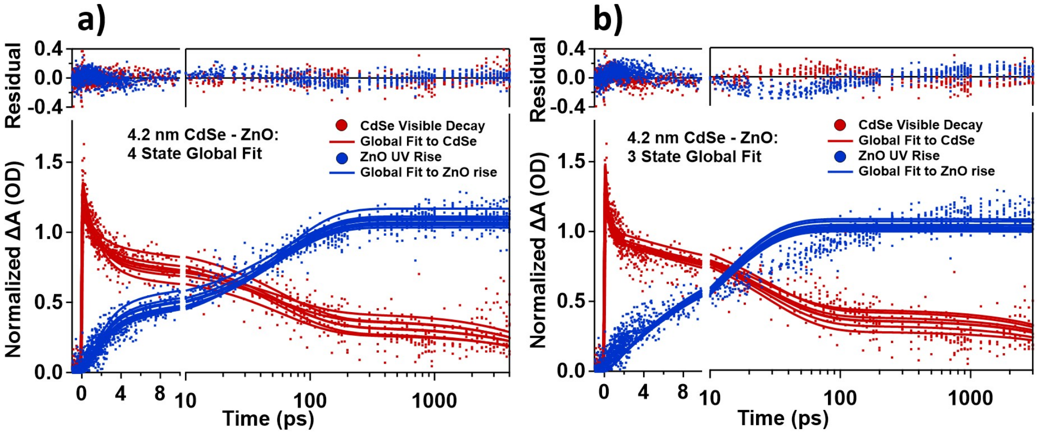

Figure 28: The a) 4 state and b) 3 state kinetic model applied to 4.2 nm CdSe@ZnO. Red data points are kinetic traces in the visible probe region at 590 nm, representing CdSe kinetics. Blue data points are taken at 365 nm and represent the ZnO kinetics. Solid lines are the fits to the individual datasets. At top are the residuals for the global fits.

all datasets, the 4-state model fits significantly better than the 3-state model, as seen in the systemic error in the residual. This is the model which is attributed to heterogeneous acceptor states. Values for these fits are reported in the main text.

References

(1) Ranjith, K. S.; Pandian, R.; Natarajan, G.; Kamruddin, M.; Rajendrakumar, R. T. *Advanced Materials Research* **2012**, *584*, 319–323.

(2) Govender, K.; Boyle, D. S.; Kenway, P. B.; O'Brien, P. *Journal of Materials Chemistry* **2004**, *14*, 2575–2591.

(3) Chambrier, I.; Banerjee, C.; Remiro-Buenamañana, S.; Chao, Y.; Cammidge, A. N.; Bochmann, M. *Inorganic Chemistry* **2015**, *54*, 7368–7380.

(4) Jasieniak, J.; Bullen, C.; Embden, J. V.; Mulvaney, P. *Journal of Physical Chemistry B* **2005**, *109*, 20665–20668.

(5) Henckel, D. A.; Enright, M. J.; Eslami, N. P.; Kroupa, D. M.; Gamelin, D. R.; Cossairt, B. M. *Nano Letters* **2020**, *20*, 2620–2624.

(6) Enright, M. J.; Cossairt, B. M. *Chemical Communications* **2018**, *54*, 7109–7122.

(7) Jasieniak, J.; Smith, L.; van Embden, J.; Mulvaney, P.; Califano, M. *The Journal of Physical Chemistry C* **2009**, *113*, 19468–19474.

(8) Leschkies, K. S.; Divakar, R.; Basu, J.; Enache-Pommer, E.; Boercker, J. E.; Carter, C. B.; Kortshagen, U. R.; Norris, D. J.; Aydil, E. S. *Nano Letters* **2007**, *7*, 1793–1798.

(9) Zhu, H.; Song, N.; Rodríguez-Córdoba, W.; Lian, T. *Journal of the American Chemical Society* **2012**, *134*, 4250–4257.

(10) Labrador, T.; Dukovic, G. *The Journal of Physical Chemistry C* **2020**, *124*, 8439–8447.

(11) Dominguez, A.; Lorke, M.; Schoenhalz, A. L.; Rosa, A. L.; Frauenheim, T.; Rocha, A. R.; Dalpian, G. M. *Journal of Applied Physics* **2014**, *115*, 203720.

(12) Greben, M.; Khoroshyy, P.; Sychugov, I.; Valenta, J. *Applied Spectroscopy Reviews* **2019**, *54*, 758–801.

(13) Hyndman, R.; Athanasopoulos, G., *Forecasting: Principles and Practice*, 3rd ed.; Otexts: 2021.

(14) Heinhold, R.; Cooil, S. P.; Evans, D. A.; Allen, M. W. *Journal of Physical Chemistry C* **2014**, *118*, 24575–24582.

(15) Mahl, J.; Gessner, O.; Barth, J. V.; Feulner, P.; Neppl, S. *ACS Applied Nano Materials* **2021**, *4*, 12213–12221.

(16) Toyoda, T.; Shen, Q.; Nakazawa, N.; Yoshihara, Y.; Kamiyama, K.; Hayase, S. *Materials Research Express* **2022**, *9*, 025005.

(17) Engelhard, M. H.; Baer, D. R.; Herrera-Gomez, A.; Sherwood, P. M. A. *Journal of Vacuum Science and Technology A: Vacuum, Surfaces, and Films* **2020**, *38*, 063203.

(18) Fang, J.; Fan, H.; Ma, Y.; Wang, Z.; Chang, Q. *Applied Surface Science* **2015**, *332*, 47–54.

(19) Neppl, S.; Mahl, J.; Roth, F.; Mercurio, G.; Zeng, G.; Toma, F. M.; Huse, N.; Feulner, P.; Gessner, O. *Journal of Physical Chemistry Letters* **2021**, *12*, 11951–11959.

(20) Leatherdale, C. A.; Bawendi, M. G. *Physical Review B - Condensed Matter and Materials Physics* **2001**, *63*, 165315.

(21) Urbach, F. *Physical Review* **1953**, *92*, 1324.

(22) Herrfurth, O.; Richter, S.; Rebarz, M.; Espinoza, S.; Zúñiga-Pérez, J.; Deparis, C.; Leveillee, J.; Schleife, A.; Grundmann, M.; Andreasson, J.; Schmidt-Grund, R. *Physical Review Research* **2021**, *3*, 013246.

(23) Zhang, C.; Zhang, F.; Xia, T.; Kumar, N.; Hahm, J.-i.; Liu, J.; Wang, Z. L.; Xu, J. *Optics Express* **2009**, *17*, 7893.

(24) Teraoka, E. Y. M.; Broaddus, D. H.; Kita, T.; Tsukazaki, A.; Kawasaki, M.; Gaeta, A. L.; Yamada, H. *Applied Physics Letters* **2010**, *97*, 071105.

(25) Yin, L.; Agrawal, G. P. *Optics Letters* **2007**, *32*, 2031.

(26) Namekawa, A.; Katoh, R. *Chemical Physics Letters* **2016**, *659*, 154–158.

(27) Baldini, E.; Palmieri, T.; Rossi, T.; Oppermann, M.; Pomarico, E.; Auböck, G.; Chergui, M. *Journal of the American Chemical Society* **2017**, *139*, 11584–11589.

(28) Stockwell, D.; Yang, Y.; Huang, J.; Anfuso, C.; Huang, Z.; Lian, T. *Journal of Physical Chemistry C* **2010**, *114*, 6560–6566.

(29) Strothkämper, C.; Bartelt, A.; Sippel, P.; Hannappel, T.; Schütz, R.; Eichberger, R. *Journal of Physical Chemistry C* **2013**, *117*, 17901–17908.

(30) Němec, H.; Rochford, J.; Taratula, O.; Galoppini, E.; Kužel, P.; Polívka, T.; Yartsev, A.; Sundström, V. *Physical Review Letters* **2010**, *104*, 197401.

(31) Gundlach, L.; Ernstorfer, R.; Willig, F. *Applied Physics A: Materials Science and Processing* **2007**, *88*, 481–495.

(32) Furube, A.; Katoh, R.; Hara, K.; Murata, S.; Arakawa, H.; Tachiya, M. *Journal of Physical Chemistry B* **2003**, *107*, 4162–4166.

(33) Furube, A.; Katoh, R.; Yoshihara, T.; Hara, K.; Murata, S.; Arakawa, H.; Tachiya, M. *Journal of Physical Chemistry B* **2004**, *108*, 12583–12592.

(34) Piersimoni, F.; Schlesinger, R.; Benduhn, J.; Spoltore, D.; Reiter, S.; Lange, I.; Koch, N.; Vandewal, K.; Neher, D. *Journal of Physical Chemistry Letters* **2015**, *6*, 500–504.

(35) N., S. B.; Němec, H.; Žídek, K.; Abdellah, M.; Al-Marri, M. J.; Chábera, P.; Ponseca, C.; Zheng, K.; Pullerits, T. *Physical Chemistry Chemical Physics* **2017**, *19*, 6006–6012.

(36) Kirmani, A. R.; Walters, G.; Kim, T.; Sargent, E. H.; Amassian, A. *ACS Applied Energy Materials* **2020**, *3*, 5385–5392.

(37) Žídek, K.; Zheng, K.; Ponseca, C. S.; Messing, M. E.; Wallenberg, L. R.; Chábera, P.; Abdellah, M.; Sundström, V.; Pullerits, T. *Journal of the American Chemical Society* **2012**, *134*, 12110–12117.

(38) Žídek, K.; Zheng, K.; Abdellah, M.; Chábera, P.; Pullerits, T.; Tachyia, M. *Journal of Physical Chemistry C* **2014**, *118*, 27567–27573.

(39) Azzaro, M. S.; Dodin, A.; Zhang, D. Y.; Willard, A. P.; Roberts, S. T. *Nano Letters* **2018**, *18*, DOI: `10.1021/acs.nanolett.8b01079`.

(40) Knowles, K. E.; Frederick, M. T.; Tice, D. B.; Morris-Cohen, A. J.; Weiss, E. A. *Journal of Physical Chemistry Letters* **2011**, *3*, 18–26.